Nanoscale

PAPER

View Article Online
View Journal | View Issue

Cite this: *Nanoscale*, 2026, **18**, 3851

3D-printed carbon nanoparticle monoliths enabling ultrahigh mass loading of NiCoAl layered double hydroxides for asymmetric supercapacitors

Jungeun Bae, Thang Cao Doan, Anisa Fitriani Rosyadi, Yebin Park and Hyojong Yoo *

Supercapacitors are promising energy storage devices due to their high power density and exceptional cycling durability. However, conventional thin-film electrodes must remain limited in thickness to avoid sluggish ion transport, thereby restricting their overall charge storage capability. To overcome this challenge, we report a three-dimensional printed electrode (3D-PE) composed of hierarchically orthogonal strings interconnected by carbon nanoparticles, serving as a robust substrate for the electrodeposition of NiCoAl-layered double hydroxide (NiCoAl-LDH@3D-PE) as the cathode in an asymmetric supercapacitor. The unique 3D-PE architecture ensures efficient ion transport, enabling the fabrication of thick, monolithic electrodes with a high mass loading of up to 28.28 mg cm^{-2} without compromising electrochemical performance. Furthermore, the role of Al in the NiCoAl-LDH framework was systematically investigated. Al incorporation enlarges the LDH interlayer spacing, thereby enhancing ion diffusion, electrochemical activity, and cycling stability. Among the tested compositions, NiCoAl-2-LDH@3D-PE (Ni : Co : Al = 1 : 1 : 0.2 in the deposition electrolyte) delivered a remarkable specific capacitance of 1968 F g^{-1} at 2.5 A g^{-1} and retained 94% of its capacity after 5000 cycles. When paired with acid-treated carbon cloth (ATCC), the NiCoAl-2-LDH@3D-PE cathode achieved an excellent areal energy density of 0.76 mWh cm^{-2} at a power density of 9.3 mW cm^{-2}. These results highlight the synergistic effect of 3D-printed electrode architectures and Al-modified NiCoAl-LDH, offering a promising pathway toward the design of high-performance monolithic electrodes for advanced supercapacitors and related electrochemical energy storage applications.

Received 11th September 2025,
Accepted 16th January 2026

DOI: 10.1039/d5nr03834k

rsc.li/nanoscale

Introduction

Supercapacitors, also known as electrochemical capacitors, are energy-storage devices that store electrical energy through electrostatic fields rather than chemical reactions in batteries.[1] Well-designed supercapacitors can have high power densities, long cycle lives, and fast charging/discharging rates, which make them ideal for applications in electric vehicles (EVs), renewable energy systems (solar and wind), consumer electronics, and industrial machinery.[2]

In commercial applications, supercapacitor electrodes are generally produced by applying a thin layer of carbon onto metal current collectors. However, the film thickness is limited by slow ion diffusion and charge transfer, which cause electrochemical performance losses as the thickness increases. Multiple thin layers can be stacked to improve the capacitance and energy density; however, this leads to an increasing weight and cost owing to the need for additional metal collectors and separators.[3] Therefore, fabricating thick monolithic (*i.e.*, single and uniform block-type) electrodes for supercapacitors is desirable.[4,5] Ruiz *et al.*[6] formed 1 mm-thick activated carbon monolith electrodes by calcinating mesophase pitch with KOH, achieving high performance for supercapacitors. To improve ion diffusion, instead of using pellets, Garcia-Gomez *et al.* fabricated 3D cylindrical carbon monoliths (1–5 mm thick) with straight channels, enabling fast electrolyte exchange and high capacitance at elevated current densities.[7] Yao *et al.* developed 2 mm-thick carbonized wood electrodes decorated with MXene, enhancing conductivity and wettability, and achieved an areal capacitance of 14.48 F cm^{-2} (203.94 F g^{-1}).[8] Ying Hu *et al.* showed that the wood-derived carbon (AWC) electrode not only serves as a template for subsequent active material loading, but also acts as an effective buffer to mitigate the volume expansion of active material during ion intercalation.[9] Recently, 3D printing has emerged as a promis-

Department of Battery and Chemical Engineering, Hanyang University, Ansan, Gyeonggi-do, 15588, Republic of Korea. E-mail: hjhaha73@hanyang.ac.kr, wjddms508@naver.com, caothangdoan@gmail.com, anisarosyadi@hanyang.ac.kr, banilla7178@hanyang.ac.kr

ing technique for fabricating hierarchical monolithic electrodes. Unlike traditional methods, it enables precise control over geometry, porosity, and mechanical strength within a single manufacturing step.[10–12] This approach offers new opportunities for designing high-performance electrodes with improved mass loading and ion transport pathways.

Layered double hydroxide (LDH) materials gain increasing attention as positive electrodes in supercapacitors due to their unique structural, electrochemical, and material properties.[13–15] In particular, ternary LDHs, such as NiCoAl-LDH represent a particularly promising approach, demonstrating superior electrochemical performance compared to their binary counterparts, such as NiAl-LDH or CoAl-LDH.[16,17] The presence of both nickel and cobalt in NiCoAl-LDH results in richer redox reactions and a higher specific capacitance. The incorporation of trivalent metal ions, especially Al^{3+}, plays a crucial role in enhancing performance. Since Al^{3+} does not undergo valence changes during cycling, it maintains the LDH's structural integrity, leading to improved long-term performance. Moreover, Al^{3+} facilitates the transformation from the β-phase to the α-phase hydroxide, increasing interlayer spacing and promoting faster ion transport. This contributes to improved charge–discharge efficiency, energy storage, and high-rate capability.[16]

Herein, 3D Printing technique was utilized to create a carbon nanoparticle monolith for electrodeposition of ternary NiCoAl-LDH as a cathode for asymmetric supercapacitors. At first, the composition of the deposited active material was optimized by the incorporation of Al into NiCoAl-LDH. Subsequently, the thickness of the monolithic electrodes was adjusted to verify the practicality of employing a 3D-PE electrode to mitigate the slow ion diffusion effect. The thick monolithic electrode with high mass loading of active material exhibits excellent areal capacitance, gravimetric capacitance, and stability. Physical characterization methods were carried out to explain the high performance of the prepared electrode. Finally, an asymmetric supercapacitor was assembled, highlighting the potential of the NiCoAl-LDH@3D-PE in creating high-performance supercapacitors.[48]

Experimental

Materials

Conductive graphene/polylactic acid (PLA) filaments were sourced from Proto-Pasta. All other chemicals, including sodium oleate; nickel nitrate hexahydrate ($Ni(NO_3)_2{\cdot}6H_2O$); nickel acetate tetrahydrate ($Ni(CH_3COO)_2{\cdot}4H_2O$, 98.0%); cobalt nitrate hexahydrate ($Co(NO_3)_2{\cdot}6H_2O$); cobalt acetate tetrahydrate ($Co(CH_3COO)_2{\cdot}4H_2O$); aluminum nitrate nonahydrate ($Al(NO_3)_3{\cdot}9H_2O$); and sodium fluoride (NaF, 99% purity), were purchased from Sigma Aldrich. Additional reagents, such as nitric acid (HNO_3, 70%), hydrogen peroxide (H_2O_2, 30%), sulfuric acid (H_2SO_4, 99.9%), and potassium permanganate ($KMnO_4$, 99.0%), were also obtained from Sigma Aldrich. All reagents were used as received without any further purification.

Preparation of 3D-PE

3D Printed electrodes (3D-PEs) were fabricated as follows: The electrode design (1 cm × 1 cm, with thicknesses of 1, 2, 3, and 4 mm) was created using Autodesk Inventor software and then moved to Sindoh software for the printing process. The 3D printing settings included a 0.1 mm layer height, a nozzle temperature of 220 °C, a bed temperature of 60 °C, and a 75% infill density. PLA carbon composite filament from Proto-Pasta was utilized for printing material, with a print speed of 60 mm s^{-1} and a filament flow rate set to 100%. Following the printing process, the electrodes were annealed at 350 °C under a nitrogen gas for 3 hours.

Surface modification of 3D-PE

The 3D-printed electrodes were modified using a nonionic surfactant treatment. In a typical procedure, 0.162 g of sodium oleate was dissolved in 40 mL of deionized water in a 100 mL flask. Four 3D-printed electrodes were immersed in this solution and maintained at room temperature (25 °C) for 24 h. After treatment, the electrodes were thoroughly rinsed with deionized water and dried at 50 °C for 12 h.

Preparation of NiCoAl-LDH@3D-PE

NiCoAl-LDH@3D-PEs electrode was prepared in 100 mL of aqueous electrolyte containing 5 mmol of each ($Ni(NO_3)_2{\cdot}6H_2O$, $Co(NO_3)_2{\cdot}6H_2O$, $Ni(CH_3COO)_2{\cdot}4H_2O$, and $Co(CH_3COO)_2{\cdot}4H_2O$) with the addition of 10 mmol NaF and 2 or 5 mmol $Al(NO_3)_3$, respectively. NiCo-LDH@3D-PE was prepared with a similar method, but without NaF and $Al(NO_3)_3$. The deposition was conducted at room temperature (~25 °C), under constant potential of −0.9 V, using a three-electrode configuration, where the 3D-printed carbon substrate served as the working electrode, Ag/AgCl (3 M KCl) as the reference electrode, and Pt wire as the counter electrode.

Fabrication of ATCC

The negative electrode ATCC (acid-treated carbon cloth) was synthesized using a slightly modified version of a previously published method.[18] Carbon cloth was first dipped in a 30 mL mixture of nitric acid and sulfuric acid (ratio 1 : 2), and heated at 60 °C for 1 hour. Afterward, potassium permanganate (1.5 g) was introduced, and the mixture was heated for 12 hours at 30 °C. Then, hydrogen peroxide (3 mL) was slowly introduced dropwise and sonicated for 1 hour. Finally, the resulting electrode was thoroughly washed several times and dried at 60 °C for 12 hours.

Characterization method

The crystal structure and phase changes of the synthesized 3D-printed electrodes were examined using X-ray diffraction (XRD, RIGAKU Ultima IV). Surface morphology of the samples was examined with scanning electron microscopy (SEM, Hitachi S-4800). Additionally, X-ray photoelectron spectroscopy (XPS, KALPHA spectrometer, Thermo VG, UK) was performed to assess the elemental composition and oxidation states of the

samples. The elemental composition of electrodes was analyzed with energy-dispersive X-ray spectroscopy (EDS, Hitachi SU 5000). The sheet resistance (RS) of uncalcinated and calcinated electrodes was directly measured using a 4-point probe technique (Jandel cylindrical four-point probe). The electrical conductivity (σ) of the electrodes was calculated according to:

$$\sigma = \frac{1}{R_S \times t \times C}$$

where t is the thickness of the electrode (cm), and C represents the geometric correction factors. Since the sufficiently large electrode dimensions ($8 \times 8 \times 0.8$ mm^3) relative to the spacing of the probes (1 mm), the geometric correction factor was taken as $C = 1$.

Electrochemical measurement

A three-electrode system was used to investigate the properties of NiCoAl-LDH@3D-PE electrodes. The respective NiCoAl-LDH@3D-PE electrode (with a geometrical area of 0.64 cm^2) was employed as the working electrode, with an Ag/AgCl electrode used as the reference and a Pt serving as the counter electrode. A range of electrochemical characterization techniques were conducted in a 6 M KOH electrolyte solution. The analytical parameters of the electrodes, including the gravimetric and areal capacitances, were calculated using eqn (1) and (2).

$$C_m = \left(2i\int V\mathrm{d}t\right)/(m\Delta V^2) \quad (1)$$

$$C_a = \left(2i\int V\mathrm{d}t\right)/(S\Delta V^2) \quad (2)$$

In there, i (A), ΔV (V), $\int V\mathrm{d}t$, and S (cm^2) represent the current in the discharge process, window potential after correcting for the IR drop, the area calculated from the discharge curve, area of the electrode, and m (g) is the mass of NiCoAl-LDH loaded on 3D-PE.

NiCoAl-LDH@3D-PE and ATCC were used as the positive and negative electrodes in an asymmetric supercapacitor. The calculated area of the AMS is 1.28 cm^2. Electrochemical characterization was performed using a 6 M KOH electrolyte solution. The energy and power characteristics of the device were calculated using the following eqn (3) and (4).

$$E_a = (C_a \times \Delta V^2)/7.2 \quad (3)$$

$$P_a = (3600E_a)/(\Delta t) \quad (4)$$

where C_a (F cm^{-2}), Δt (s), ΔV (V) correspond to the areal capacitance, discharge time, and the operating voltage window, respectively. IR compensation was not applied in real time during the three-electrode measurements. The *iR* drop was corrected using the internal resistance (equivalent series resistance, R_{esr}) obtained from electrochemical impedance spectroscopy (EIS) at the high-frequency intercept. The measured potential (V_{meas}) during the discharge process was corrected (V_{corr}) according to

$$V_{corr} = V_{meas} - I \times R$$

where I is the applied current. The potential window was chosen from the onset of the linear discharge region to the end of the discharge curve after excluding the initial instantaneous voltage drop (*iR* drop) and the final nonlinear tail.

Results and discussion

Electrode preparation process

The fabrication process for NiCo-LDH@3D-PE. A PLA/graphite filament was used to fabricate the electrode using FDM 3D printing (Scheme 1). Thermal annealing is employed to enhance the conductivity of the 3D-printed electrodes. Under 350 °C, the PLA portion is decomposed, resulting in the formation of a graphitized skeleton electrode composed of interconnected carbon nanoparticles. The electrical conductivity of the uncalcinated and calcinated electrodes was 0.005 and 0.048 S cm^{-1}, respectively, confirming the significant enhancement in electrical conductivity after the calcination step. To facilitate the electrodeposition, the graphitized electrode surface was treated with sodium oleate. The hydrophobic functional groups of sodium oleate are attached to the electrode surface, changing hydrophobic nature of the carbon-based electrode to hydrophilic.[19] Finally, ternary NiCoAl-*x*-LDH nanosheets were grown on the surface-modified 3D-printed

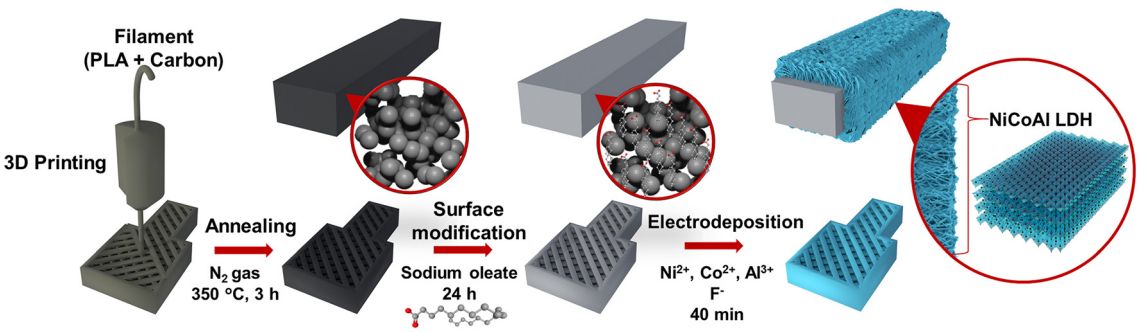

Scheme 1 Diagram depicting the preparation of NiCoAl-LDH@3D-PE.

electrodes through electrodeposition. Due to the significant difference in the solubility constants of the corresponding hydroxides, $Al(OH)_3$ is preferentially deposited over $Ni(OH)_x$ or $CO(OH)_x$. Therefore, NaF was introduced into the deposition electrolyte, where F^- ions formed complexes with Al^{3+}. Consequently, Al^{3+} was slowly and controllably released from these complexes, resulting in uniform NiCoAl-*x*-LDH deposition onto the 3D printed electrodes.

Characterization of NiCoAl-*x*-LDH@3D-PEs

Scanning electron microscopy (SEM) images of the NiCoAl-*x*-LDH@3D-PEs are presented in Fig. 1.

The structure of a monolithic 3D-printed electrode (Fig. 1a and b) consists of orthogonally stacked parallel strings forming a multilayer carbon framework. This structure allows electron transport both within and between the plates *via* interconnected layers. The space between the plates and layers facilitates electrolyte ion transportation. Fig. 1c presents a high-magnification SEM image of the 3D-PE, revealing that each printed string is composed of interconnected carbon nanoparticles, which form nanoscale pores between them. After electrodeposition, NiCo-LDH nanosheets with layered structures are observed on the electrode surface (Fig. 1e and j). With the addition of Al, the NiCoAl-2-LDH@3D-PE became denser (Fig. 1g and k). The observed densification and compaction in NiCoAl-2-LDH@3D-PE upon Al addition suggest an increase in the active surface area, providing more electrochemically accessible sites and enhanced electrolyte contact. To provide quantitative evidence supporting the increase in active surface area after Al incorporation, N_2 adsorption–desorption (BET) analysis was conducted (Fig. S8). The measured BET surface area of NiCo-LDH was 12.46 $m^2\ g^{-1}$, while that of NiCoAl-2-LDH@3D-PE increased significantly to 18.67 $m^2\ g^{-1}$ (Table S1). This confirms that Al incorporation not only modi-

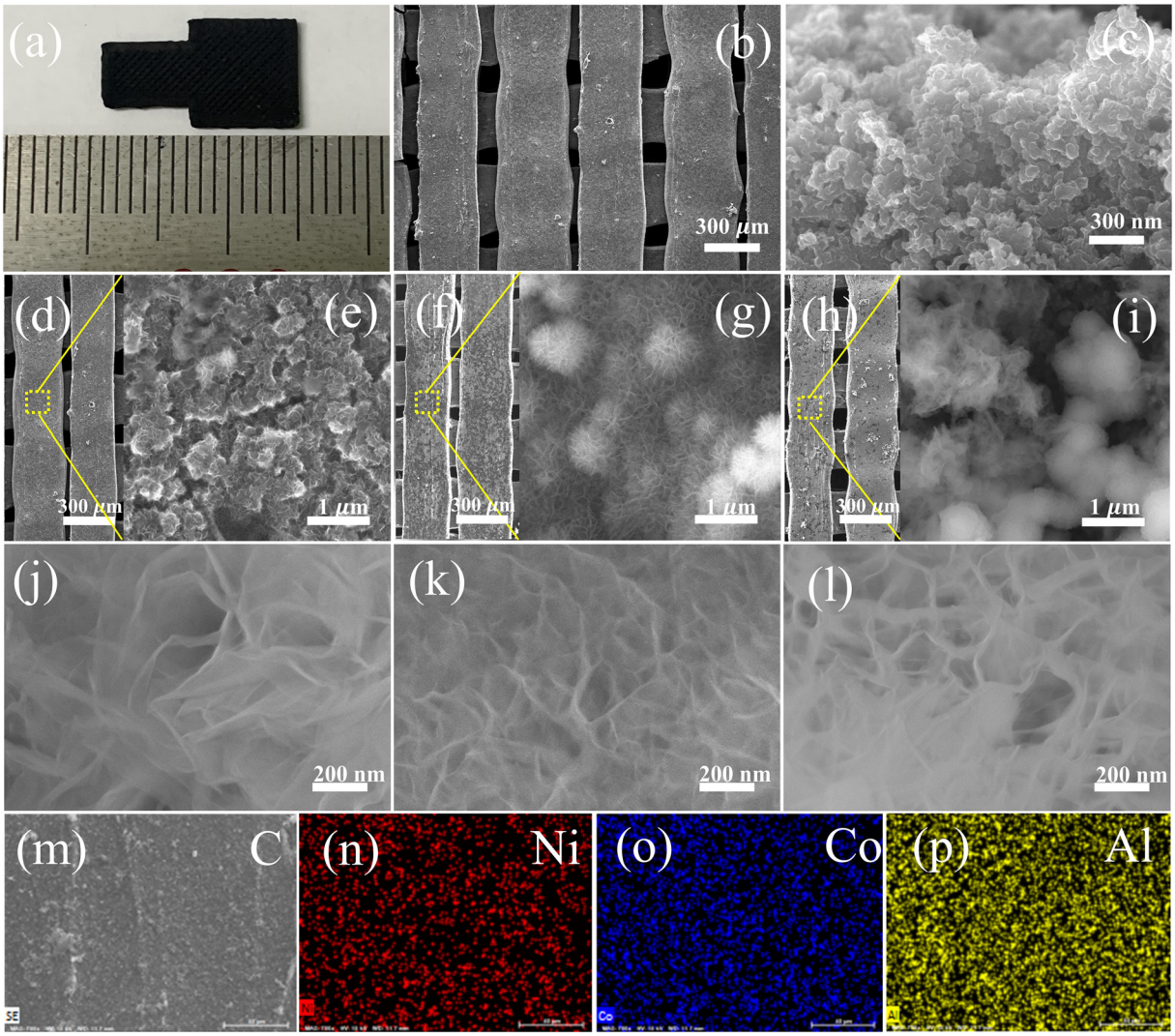

Fig. 1 (a) Digital image, (b) SEM image at low magnification, and (c) SEM image at high magnification of 3D-PE; (d–l) SEM images of (d, e, and j) NiCo-LDH@3D-PE, (f, g, and k) NiCoAl-2-LDH@3D-PE, (h, i and l) NiCoAl-5-LDH@3D-PE; (m–p) Elemental mapping distribution for ((m) C, (n) Ni, (o) Co, and (p) Al) of NiCoAl-2-LDH@3D-PE.

fied the nanosheet morphology but also enhanced porosity and electrolyte-accessible area. The morphology of NiCoAl-5-LDH@3D-PE (Fig. 1i and l) is similar to NiCoAl-2-LDH@3D-PE, but with clumps on the LDH layer. The clumps observed for NiCoAl-5-LDH@3D-PE likely resulted from the increased Al content in the electrolyte. The resulting decrease in the F^- to Al^{3+} ratio favors the release of Al^{3+}, leading to the observed particle-like morphology.[20] EDS mapping (Fig. 1m–p) reveals a uniform spreading of Ni, Co, Al, C, and O on the NiCoAl-2-LDH@3D-PE surface. Cross-sectional elemental mapping (EDS) analysis was performed to confirm the distribution of Ni, Co, and Al elements within the carbon matrix. As shown in Fig. S1, the EDS mapping demonstrates a uniform distribution of elements throughout the 3D-printed carbon framework, confirming the successful deposition of LDH layer.

XRD analysis was conducted to investigate the crystalline characteristics of NiCoAl-*x*-LDH@3D-PE. As shown in Fig. 2a, the XRD pattern of 3D-PE exhibits a wide diffraction peak, indicating the amorphous configuration of PLA.[21] For NiCo-LDH@3D-PE, the peaks observed at 11.3°, 33.4°, and 59.5° correspond to the (003), (102), and (110) crystal planes of Ni $(OH)_2{\cdot}0.75H_2O$ within the hydrotalcite structure (JCPDS #38–0715).[22] Meanwhile, the peaks of $Co(OH)_2$ appeared at 9.5°, 19.2°, 38.0°, and 58.2°, attributed to the (001), (002), (102), and (110) planes (JCPDS #51–1731), respectively.[23] NiCoAl-2-LDH@3D-PE and NiCoAl-5-LDH@3D-PE exhibit nearly identical diffraction peaks at 2θ angles of 11.5°, 23.0°, 34.0°, 39.0°, 46.0°, 60.0°, and 61.0°. These peaks correspond to the (003), (006), (012), (015), (018), (110), and (113) planes of the α-phase NiCoAl-LDH structure (JCPDS# 15-0087),[24] although some weak reflections such as (006), (015), and (104) are not distinctly visible. This can be attributed to the low crystallinity of the nanosheet-like LDH structure.[16,25]

The incorporation of aluminum ions into the LDH structure is confirmed by the formation of a hydrotalcite-like structure.[26] The intensity of the peak (001) at 9.5° for NiCo-LDH@3D-PE, which corresponds to $Co(OH)_2$, becomes lower in the XRD pattern of NiCoAl-2-LDH@3D-PE and almost disappears in NiCoAl-5-LDH@3D-PE pattern. Meanwhile, the intensity of the (003) peak at 11.5° increases with the incorporation of aluminum, indicating that the crystallinity is enhanced by introducing Al^{3+} into the transition metal hydroxide layer.[24] This feature also confirms the partial substitution of nickel or cobalt ions with aluminum ions in the octahedral hydroxide structure. From the peak (003), using Bragg's law, the interlayer spacing of NiCoAl-2-LDH@3D-PE and NiCoAl-5-LDH@3D-PE are 7.72 Å and 7.74 Å, which are enlarged compared to NiCo-LDH@3D-PE (7.60 Å). This expansion in interlayer spacing facilitates rapid ion transport.[27] Notably, while NiCoAl-2-LDH@3D-PE exhibits a pure LDH phase, NiCoAl-5-LDH@3D-PE shows a small amount of $Al(OH)_3$ impurities at a peak position of 17.77° in addition to the LDH phase.[16] This suggests that the LDH phase becomes saturated with metal ions as the concentration of Al^{3+} ions increases. Consequently, any excess Al introduced beyond this saturation point leads to the formation of $Al(OH)_3$.

X-ray photoelectron spectroscopic investigations were conducted on NiCo-LDH@3D-PE (Fig. S1), NiCoAl-2-LDH@3D-PE (Fig. 2b–e), and NiCoAl-5-LDH@3D-PE (Fig. S2) to further elucidate their surface characteristics. The Ni core level spectra feature two spin–orbit doublets, Ni $2p_{3/2}$ and Ni $2p_{1/2}$, accompanied by two satellite peaks. The peaks detected at

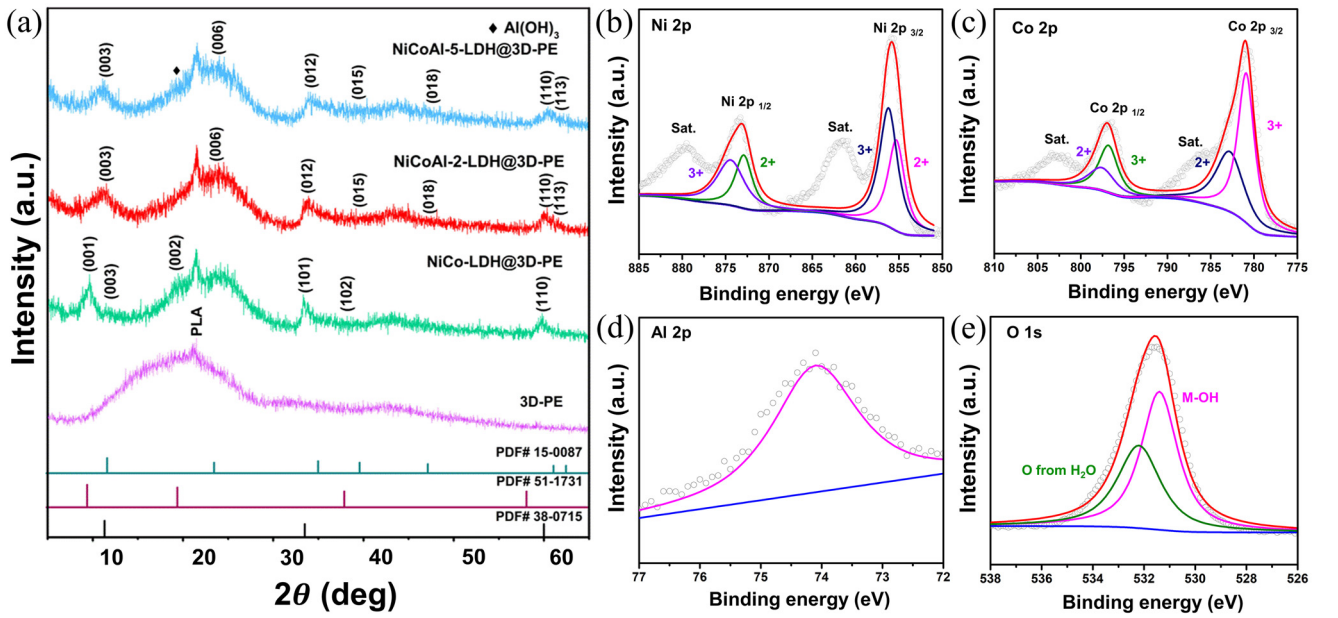

Fig. 2 XRD patterns for 3D-PE, NiCo-LDH@3D-PE, NiCoAl-LDH-2@3D-PE and NiCoAl-LDH-5@3D-PE (a). The high-resolution XPS spectra of Ni 2p (b), Co 2p (c), Al 2p (d), and O 1s (e) for NiCoAl-LDH-2@3D-PE.

binding energies of 855.3 eV and 872.9 eV confirm the presence of Ni^{2+}, whereas those at 856.2 eV and 874.5 eV correspond to Ni^{3+} (Fig. 2b).[28] The Co 2p spectrum (Fig. 2c) exhibits two distinct pairs of doublets, corresponding to Co $2p_{3/2}$ and Co $2p_{1/2}$. The peaks at 782.9 eV and 797.7 eV are credited to Co^{3+}, while the binding energies at 780.9 eV and 796.0 eV correspond to Co^{2+}.[29] The peak observed at a binding energy of 74.1 eV in the Al 2p spectra (Fig. 2d) is attributed to the presence of Al^{3+} species.[30] High-resolution O 1s X-ray photoelectron spectroscopy (XPS) analysis shows two distinct peaks at binding energies of 531.4 eV and 532.2 eV. These spectral features can be attributed to the presence of hydroxyl (OH) groups associated with metal-hydroxyl (M–OH) species and adsorbed water molecules on the surface of the material. Fig. S2 and S3 show negligible differences in the XPS peaks of NiCo-LDH@3D-PE and NiCoAl-5-LDH@3D-PE, indicating similar electronic structures.

Raman spectroscopy was employed to evaluate the graphitization and structural changes of the 3D-printed carbon scaffold before and after LDH deposition (Fig. S4). The bare 3D-PE shows two prominent peaks: the D band at 1350 cm^{-1}, associated with disordered carbon or defects, and the G band at 1595 cm^{-1}, corresponding to graphitic sp^2 carbon. The calculated I_D/I_G ratio of 0.81 indicates a partially graphitized scaffold with a relatively low defect density, retaining a good fraction of ordered sp^2 carbon domains, which can be advantageous for electronic conductivity. After deposition of NiCoAl-LDH, the Raman spectrum of NiCoAl-LDH@3D-PE shows a minor increase in the I_D/I_G ratio to 0.95. The increase in the I_D/I_G ratio after LDH deposition is mainly attributed to interfacial disorder induced by the nucleation and growth of LDH on the carbon surface; minor surface oxidation of the carbon scaffold during the aqueous electrodeposition process may also contribute, but it is expected to be limited. These results confirm that the 3D-PE maintains a conductive framework while the LDH deposition slightly increases surface disorder, which may enhance electrolyte wettability and electrochemical performance.[31,32]

Electrochemical performance

Electrochemical properties of the fabricated NiCoAl-LDH@3D-PEs. The 0.8 mm-thick NiCo-LDH@3D-PE, NiCoAl-2-LDH@3D-PE, and NiCoAl-5-LDH@3D-PE electrochemical properties were assessed as working electrodes in a three-electrode setup with 6 M KOH electrolyte. As shown in Fig. 3a (dotted lines), the thermally treated 3D-PE electrodes exhibit negligible electrochemical activity. However, the subsequent surface modification and electrodeposition of NiCo-LDH significantly improve its electrochemical performance, as evidenced by the cyclic voltammogram (CV) of NiCo-LDH@3D-PE (Fig. 3a, dashed-dotted line). NiCo-LDH@3D-PE electrode exhibits two distinct peaks, indicating the occurrence of faradaic redox reactions. NiCoAl-2-LDH@3D-PE electrode demonstrates greater enclosed curve areas than those of the NiCo-LDH@3D-PE, indicating enhanced areal capacitance properties for the NiCoAl-2-LDH@3D-PE system (Fig. 3a, solid line).

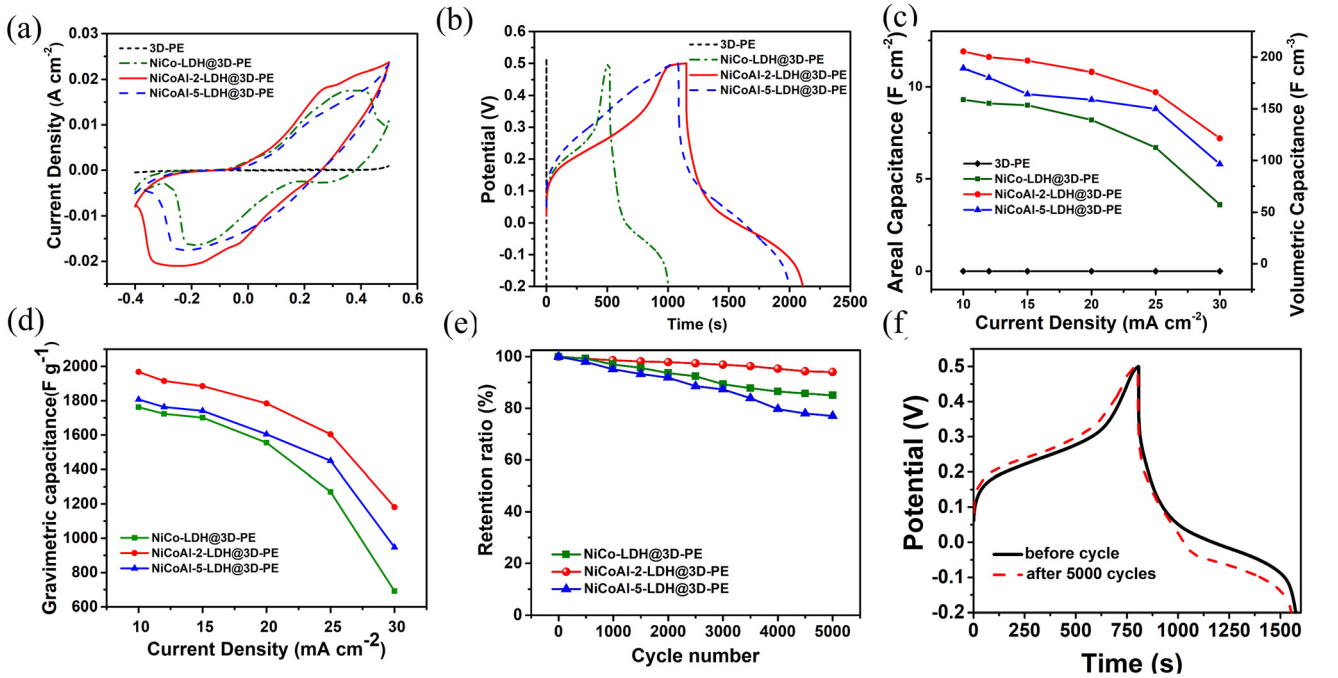

Fig. 3 (a) CV curves and (b) GCD curves of 3D-PE (short dash line), NiCo-LDH@3D-PE (solid line), NiCoAl-LDH-2@3D-PE (dash line), and NiCoAl-LDH-5@3D-PE (dash dot line). Diagram illustrating the relationship between areal and volumetric (c) and gravimetric capacitance (d) at varied current densities. (e) Cycling test of NiCoAl-LDH@3D-PEs with varying Al content. (f) GCD curves of NiCoAl-2-LDH@3D-PE pre and post 5000 cycles (10 mA cm^{-2}).

The GCD curves obtained at a current density of 10 mA cm^{-2} were further examined and are shown in Fig. 3b and Fig. S9c–e. The presence of two distinct plateaus in the galvanostatic charge–discharge curves of the NiCo-LDH@3D-PE, NiCoAl-2-LDH@3D-PE, and NiCoAl-5-LDH@3D-PE electrodes corresponds well with the observation of two redox peaks in their respective cyclic voltammetry profiles. The performance of NiCo-LDH@3D-PE, NiCoAl-2-LDH@3D-PE, and NiCoAl-5-LDH@3D-PE electrodes indicates their capacitive role in the energy storage mechanism of the assembled electrode system. The NiCoAl-2-LDH@3D-PE electrode exhibits the longest discharge time among all fabricated electrodes. Fig. 3c presents the areal capacitance values of different electrodes across a range of current densities, revealing that the NiCoAl-2-LDH@3D-PE exhibits a significantly higher areal capacitance than the other electrodes, ranging from 7.2 to 11.9 F cm^{-2}. In contrast, the NiCoAl-5-LDH@3D-PE, with its higher aluminum content, shows a reduced areal capacitance (6.3–11 F cm^{-2}). It's important to note that aluminum itself is electrochemically inactive and does not directly contribute to charge storage.[33] Consequently, excessive Al content can hinder charge storage and reduce the overall areal capacitance. Therefore, optimizing the Al content is crucial for balancing the enhanced ion transport with the charge storage capacity for optimal electrochemical performance.

In Fig. 3d, which shows the gravimetric capacitances of the electrodes at different discharge current densities. At a current density of 10 mA cm^{-2}, the gravimetric capacitances for the NiCo-LDH@3D-PE, NiCoAl-2-LDH@3D-PE, and NiCoAl-5-LDH@3D-PE electrodes are measured as 1762, 1968, and 1807 F g^{-1}, respectively. As the current density increased to 30 A g^{-1}, the specific capacitances decreased to 692, 1518, and 1030 F g^{-1}, with corresponding capacitance retention rates of 39.2%, 77.1%, and 57.0%. These results reinforce the finding that incorporating Al in an appropriate proportion can significantly enhance the gravimetric capacitance and rate performance. This enhancement can be attributed to the enlargement of α-NiCoAl-*x*-LDHs, which exhibit larger interlayer spacings that improve electrochemical kinetics by enhancing the intercalation and deintercalation of OH^- anions, thus improving structural stability during cycling.[11] Fig. 3e illustrates the cycling stability of the four different electrodes over 5000 charge/discharge cycles. After 5000 cycles, the capacitance retentions are recorded as follows: 85% for NiCo-LDH@3D-PE, 94% for NiCoAl-2-LDH@3D-PE, and 77% for NiCoAl-5-LDH@3D-PE. This enhanced stability is attributed to the robust morphology of the NiCoAl-2-LDH@3D-PE electrode, as evidenced by the minimal changes observed in the galvanostatic charge–discharge curves between the 1st and 5000th cycles (Fig. 3f). This superior electrochemical performance, including high capacitance retention, is attributed to the increased active surface area of the NiCoAl-2-LDH@3D-PE electrode material, which facilitates more efficient charge storage and transfer. These results confirm the successful electrodeposition of NiCoAl-*x*-LDH onto the 3D-printed electrode. Among the other materials, NiCoAl-2-LDH@3D-PE exhibited the best areal capacitance, gravimetric capacitance, and stability, and was used for further experiments.

The CVs were measured at various scan rates (*e.g.*, 0.2–1 mV s^{-1}) to evaluate the charge-storage mechanism (Fig. S5a). The relationship between peak current (i) and scan rate (ν) was analyzed using the power-law equation $i = a\nu^b$. The calculated b-value is 0.79, indicating a mixed charge-storage behavior involving both diffusion-controlled and surface-capacitive processes (Fig. S5b). Furthermore, the capacitive and diffusion-controlled contributions were quantified using the equation $i = k_1\nu + k_2\nu^{1/2}$, and the results (Fig. S5c) show that the diffusion-controlled contribution increases with scan rate, due to the limitation of diffusion time. To investigate the charge storage mechanism, electrochemical impedance spectroscopy (EIS) was performed, and the results were fitted using an equivalent circuit model (Fig. S6). The Nyquist plots show a semicircle in the high-frequency region corresponding to the charge-transfer resistance (R_{ct}) and a straight line in the low-frequency region related to ion diffusion. The NiCoAl-2-LDH@3D-PE electrode exhibits the smallest R_{ct} value (3.96 Ω) compared to the NiCo-LDH@3D-PE electrode (15.5 Ω) and the NiCoAl-5-LDH@3D-PE electrode (8.07 Ω), indicating faster charge-transfer kinetics and enhanced interfacial conductivity due to Al incorporation. These results further support the improved electrochemical performance of the NiCoAl-LDH-based electrode.

To validate the capability of the unique 3D-printed structure to form a monolithic electrode capable of hosting a large amount of active material without causing limited ion transport, the electrode thickness was varied from 0.8 mm to 1.6, 2.4, and 3.2 mm by stacking 10, 20, and 30 orthogonal 3D-printed layers, respectively, aiming to increase areal capacitance without compromising gravimetric performance – an indication that ion diffusion remains efficient. A consistent 40 min NiCoAl-LDH electrodeposition time was used for all electrodes, resulting in mass loadings of 9.06, 14.06, 18.75, and 28.12 mg cm^{-2} to electrodes with thicknesses of 0.8, 1.6, 2.4, and 3.2 mm, respectively. Fig. 4a and b display the GCD and CV curves for NiCoAl-LDH@3D-PE at varying electrode thicknesses, respectively.

As the electrode thickness increases, the CV curves of NiCoAl-2-LDH@3D-PE electrodes exhibit progressively larger enclosed areas, indicating an improvement in areal capacitance resulting from increased utilization of active material (Fig. 4a). An increase in the NiCoAl-2-LDH@3D-PE electrode thickness leads to longer charge–discharge durations, indicating enhanced areal capacitance. Fig. 4b, Fig. S10, and Table 1 present the corresponding areal capacitance values for different electrode thicknesses. As the electrode thickness increases from 0.8 to 3.2 mm (4 times), the capacitance at a current density of 10 mA cm^{-2} increased significantly from 12.1 to 49.9 F cm^{-2} (≈4 times). At a higher current density of 30 mA cm^{-2}, the areal capacitance is maintained at 87.9% of its value at 10 mA cm^{-2}. Fig. 4c shows the areal capacitance of electrodes with varying thicknesses. The areal capacitance increases linearly with electrode thickness. Importantly, the gravimetric capacitance remains relatively constant despite the

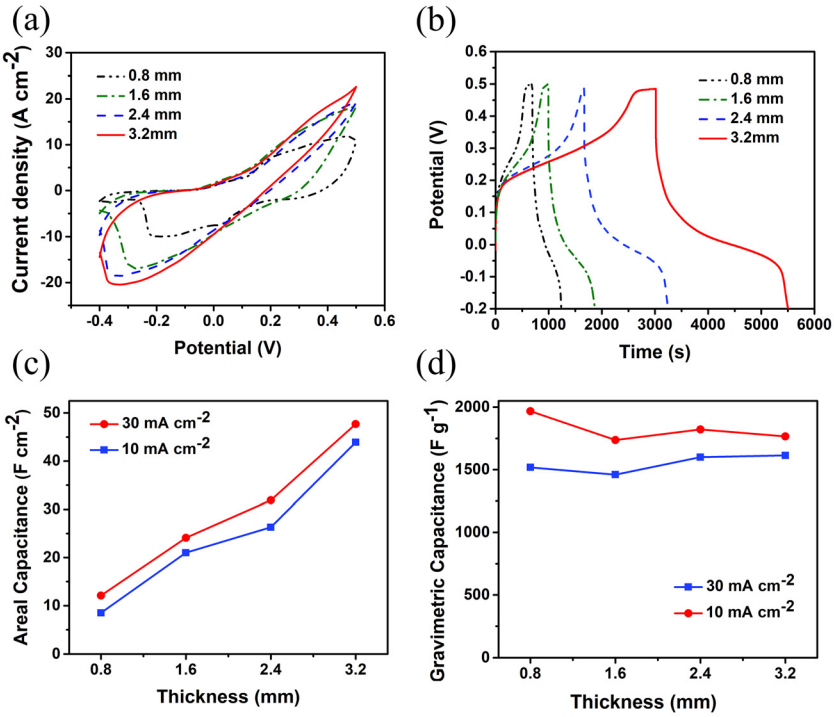

Fig. 4 NiCoAl-LDH@3D-PE performance at various electrode thicknesses: CV profile of NiCoAl-LDH@3D-PEs at 1 mV s^{-1} (a), GCD curves at a current density of 10 mA cm^{-2} (b), areal capacitance (c), gravimetric capacitance (d).

Table 1 NiCoAl-LDH@3D-PE performance at varying electrode thicknesses

Thickness (mm)	Mass loading (mg cm^{-2})	Areal capacitance (F cm^{-2})	Capacitance (F g^{-1})
0.8	9.06	12.1	1968
1.6	14.06	24.1	1737
2.4	18.75	31.9	1774
3.2	28.12	49.9	1766

changes in electrode thickness (Fig. 4d). This contrasts with traditional electrodes, where increasing thickness often leads to a decrease in capacitance. In those cases, ion transport limitations hinder access to the deeper regions of the electrode, effectively reducing the active surface area and thus the capacitance. The 3D-PE structure mitigates this capacitance reduction through its unique architecture. The porous structure of the 3D-PE facilitates efficient ion diffusion throughout the electrode, even with increasing thickness. This ensures that a larger portion of the active material remains accessible for charge storage, maintaining high gravimetric capacitance. The 3D-PE's uniform construction of orthogonal layers further enhances ion transport. This architecture exposes the active material and supports efficient diffusion to the electrode surface. The performance of NiCoAl-LDH electrodeposited on 3D-printed electrodes (3D-PE) was evaluated under various thickness and mass loading conditions, and the results of comparative analysis with other NiCo-LDH and NiCoAl-LDH-based materials are summarized in Table 2. NiCoAl-2-LDH@3D-PE demonstrates superior areal and gravimetric capacitances compared to the other materials. This suggests that the 3D-PE structure not only enables a high mass loading of active materials but also provides efficient diffusion pathways for electrolyte ions, thus maintaining a high capacitance even in thick electrodes. The corresponding Nyquist plots and fitted equivalent circuit models have been showed in Fig. S11, and Table S2. The decrease in R_{esr} with thicker scaffolds can be attributed to the enhanced electrical conductivity of the bulk carbon framework. As the 3D-printed scaffold becomes thicker, the interconnected conductive network improves the electron transport pathways, thereby lowering the intrinsic series resistance. In contrast, the R_{ct} value slightly increased with increasing electrode thickness. The thicker scaffold likely extends the ion transport pathways and enhances pore tortuosity, which can impede electrolyte penetration into inner active sites and slightly raise the interfacial impedance. This moderate increase in R_{ct} correlates well with the slight decrease in capacitance, as shown in Fig. 4d and Table 2. However, the capacitance reduction is only about 10%, confirming the high efficiency and well-designed architecture of the 3D-printed scaffold in maintaining effective ion and electron transport. Fig. S14 schematically illustrates the ion and electron transport pathways within the 3D-printed electrode. While the LDH with Al incorporation enlarges the interlayer spacing, accelerating ion diffusion, the 3D carbon framework provides efficient electron conduction channels. The combination of these features ensures effective electrochemical utilization of the active material.

Table 2 Capacitance and mass loading comparison between NiCoAl-LDH@3D-PE and related material-based substrates

Electrode	Mass loading (mg cm^{-2})	Capacitance	Ref.
4M-P@NiCo-LDH@Ni foam	4	7 F cm^{-2} at 50 mA cm^{-2}	35
Cu_2S@NiCo-LDH@Cu foam	5	20.4 F cm^{-2} at 4 mA cm^{-2}	29
s-NiCo-LDH@C cloth	5.85	7.73 F cm^{-2} at 5 mA cm^{-2}	36
Ni-P@NiCo LDH@Ni foam	2.37–2.74	12.9 F cm^{-2} at 5 A g^{-1}	37
NiCoAl-LDH/$V_4C_3T_x$	2	1445 F g^{-1} at 2 A g^{-1}	30
$NCAF_5$	1.5	1542.2 F g^{-1} at 1 A g^{-1}	20
$NiCo_2$Al-LDH	8.5	882 F g^{-1} at 1 A g^{-1}	38
rGO@NiCoAl-LDHs	5	2291.6 F g^{-1} at 1 A g^{-1}	39
NiCo-LDH@3D-PE (1.6 mm)	15.3	25.9 F cm^{-2} at 10 mA cm^{-2}	15
MnO_2@WC (0.8 mm)	75	55.4 F g^{-1} at 1 mA cm^{-2} 4.2 F cm^{-2} at 1 mA cm^{-2}	40
WC@Ag@$NiCo_2S_4$ (0.8 mm)	46.7	6.1 F cm^{-2} at 50 mA cm^{-2}	41
3D GO/MnO_2 (4 mm)	182.2	44.1 F cm^{-2} at 0.5 mA cm^{-2}	10
NiCo-LDH/MnO_2@NDC	—	21.56 F cm^{-2} at 10 mA cm^{-2}	42
NiCo-LDH@$NCW_{1.0}$-12	71.7	65.38 F cm^{-2} at 10 mA cm^{-2}	43
NiCoAl-2-LDH@3D-PE (0.8 mm)	9.06	1968 F g^{-1} at 1.1 A g^{-1} 12.1 F cm^{-2} at 10 mA cm^{-2} 151.3 F cm^{-3} at 10 mA cm^{-2}	**This work**
NiCoAl-2-LDH@3D-PE (3.2 mm)	28.28	1766 F g^{-1} at 0.4 A g^{-1} 49.9 F cm^{-2} at 10 mA cm^{-2} 149.4 F cm^{-3} at 10 mA cm^{-2}	**This work**

To investigate the reason behind the efficient ion diffusion of the electrode at high mass loading, physical characterization was conducted. The cross-sectional image of the electrode (Fig. 5a) reveals an ordered multilayer structure, where layers are stacked to form horizontal channels that facilitate the free movement of electrolyte ions within the electrode. Each layer consists of orthogonally arranged strings, which enable electron transport along the strings and between layers through their contact points. The porous, ordered structure allows electrolyte ions to easily penetrate and interact with the LDH layers.

As shown in Fig. 5b, vertical LDH nanosheets are observed on the surface of a string. Initially, the string is composed of a composite material made of PLA and carbon-based particles. After calcination, the PLA decomposes, leaving behind a structure of interconnected carbon particles. To determine whether LDH layers also formed within the string over carbon particles, the material was ground for examination. Interestingly, Fig. 5c reveals a crystalline LDH layer (within the dark blue region) covering amorphous carbon-based particles (within the red region). Inset Fig. 5c shows the crystal lattice of 0.302 nm, which corresponds to the (100) plane of NiCoAl-LDH, consistent with previous reports.[25,34] At higher magnification, Fig. 5d clearly displays a single carbon-based particle coated with a thin crystalline LDH layer. To confirm the presence of LDH within the strings, porosity measurements were performed before and after LDH deposition. Fig. 5e shows nitrogen adsorption isotherm of 3D-PE, which shows a higher adsorption capacity than NiCoAl-LDH@3D-PE. The interconnected carbon-based structure exhibits a high BET surface area of 41.04 m^2 g^{-1}, a large pore volume of 0.15 m^3 g^{-1} and a mean pore diameter of 14.46 nm, an ideal architecture for electrodeposition (Table S1). After LDH deposition, the NiCoAl-LDH@3D-PE sample shows a reduced BET surface area of 18.67 m^2 g^{-1} and a pore volume of 0.05 cm^3 g^{-1}. This significant reduction confirms the infiltration of LDH layers into the pores of the carbon-based network. Additionally, the BJH pore size distribution curve (Fig. 5f) shows a marked decrease in pore volume for NiCoAl-LDH@3D-PE compared to 3D-PE, further supporting the conclusion that LDH layers have been deposited within the porous structure. Overall, the results indicate that LDH layers are not only formed on the electrode surface but are also uniformly deposited along each printed string and even within the strings, filling the pores of the interconnected carbon-based structure. This uniform distribution prevents the formation of stacked or overly thick LDH layers at high mass loading, thereby eliminating slow ionic kinetics.

NiCoAl-LDH@3D-PE//ATCC asymmetric supercapacitor device. An asymmetric supercapacitor device was assembled to further demonstrate the potential applications of the NiCoAl-LDH@3D-PE electrodes. When NiCoAl-LDH@3D-PE is battery-type materials, the device requires an anode with fast hydroxide ion transport to maximize the power density and operating voltage. Acid-treated carbon cloth is considered a suitable anode material owing to its enhanced ion transport properties. To evaluate its electrochemical behavior, a three-electrode system was employed to investigate the kinetic parameters of ATCC before assembling the fully asymmetric device.

The cyclic voltammetry curves of the acid-treated carbon cloth electrode at various scan rates (5 to 30 mV s^{-1}) are presented in Fig. S12a. The CV curve at 5 mV s^{-1} exhibits a distinct rectangular shape, indicating a typical electric double-layer capacitance behavior. Furthermore, the CV curves consistently display a quasi-rectangular shape without any noticeable redox peaks across all scan rates, suggesting the presence of pseudocapacitive behavior in the asymmetric supercapacitor. With increasing scan rate, the capacitance also increases, indicating efficient electrolyte ion insertion and

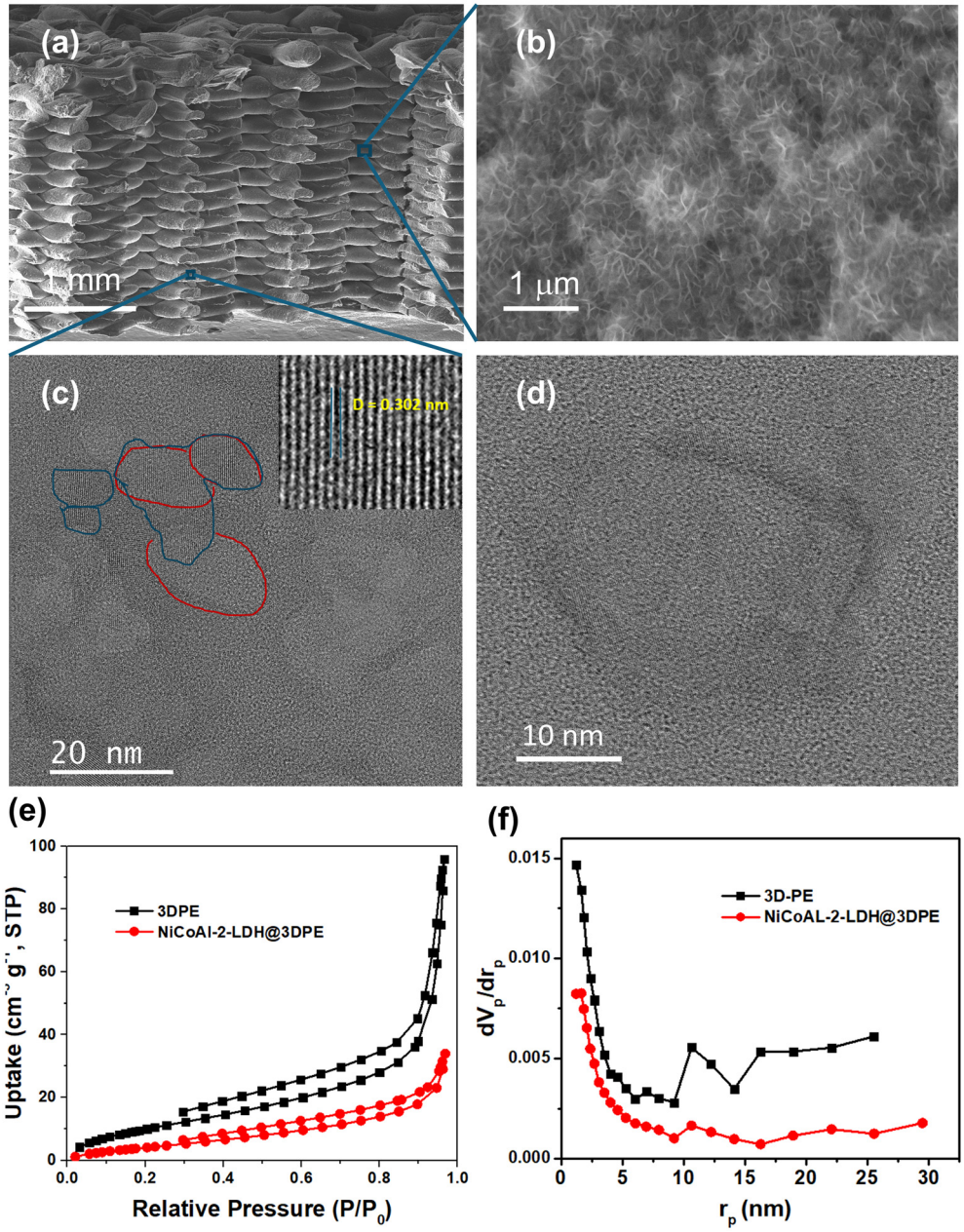

Fig. 5 SEM image of NiCoAl-2-LDH@3DPE at (a) crossectional position; (b) surface position of 3D printed string inside electrode; (c and d) TEM image of ground NiCoAl-2-LDH@3DPE particles inside 3D Printed string at average (c) and (d) higher magnification. Nitrogen adsorption isotherm (e) and BJH curve (f) of NiCoAl-2-LDH@3DPE.

extraction. Further examination of the galvanostatic charge–discharge curves for the ATCC electrode revealed a triangular profile, which validates the enhanced capacitance performance of ATCC at the applied current levels (Fig. S12b). The areal capacitance values of the acid-treated carbon cloth electrode at varying current densities are 3.1, 3, 3, 2.8, 2.7, and 2.6 F cm^{-2} (Fig. S12c). Additionally, the Nyquist plot of the acid-treated carbon cloth electrode exhibits a low charge transfer resistance of 4.7 Ω (Fig. S12d).

NiCoAl-2-LDH@3D-PE and ATCC were used as the positive electrode and negative electrode for the fabrication of an asymmetric supercapacitor, both having an identical geometric area of 0.64 cm^2. These electrodes exhibit operating potential windows of −0.2 to 0.5 V and −1.2 to −0.2 V, respectively. Based on these individual potential windows, the appropriate potential window for the assembled NiCoAl-2-LDH@3D-PE// ATCC asymmetric supercapsitor is determined from 0 to 1.7 V. Cyclic voltammetry tests performed on the NiCoAl-LDH@3D-PE//ATCC at different scan rates reveal the changes in the CV curve shape with increasing scan rate, indicating improved rate capability and capacitance performance (Fig. 6a). The galvanostatic charge–discharge curves obtained

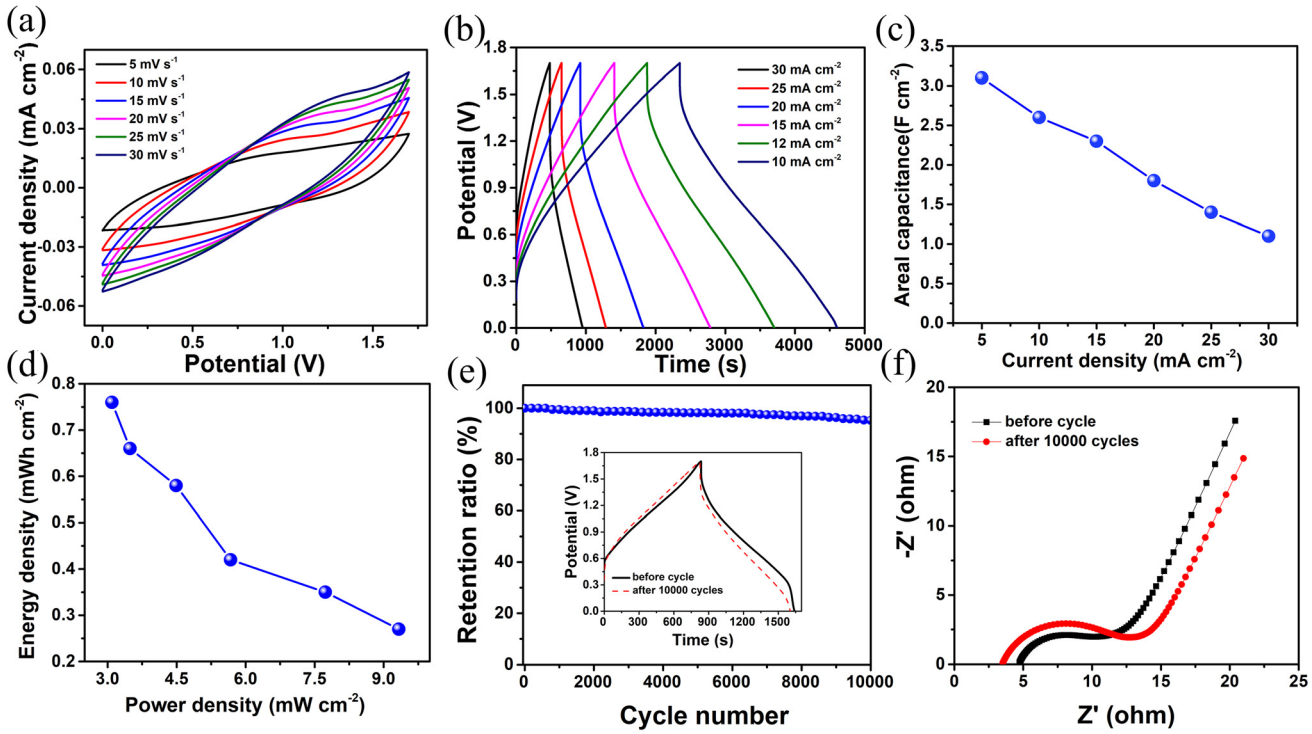

Fig. 6 Properties of NiCoAl-LDH@3D-PE//ATCC device: (a) CV curves at different scan rates, (b) GCD curves at different current densities, (c) areal capacitance of the device, (d) Ragone diagram, (e) Cycle tests (100 mA cm^{-2}) and GCD profiles recorded (10 mA cm^{-2}) pre and post cycling are inserted. (f) EIS measurement pre- and post-stability test.

at various current densities (Fig. 6b) show symmetrical triangular shapes, indicating ideal capacitive behavior. Fig. 6c presents the areal capacitance at current densities ranging from 5 to 30 mA cm^{-2}, measured at 3.1, 2.6, 2.3, 1.8, 1.4, and 1.1 F cm^{-2}. Ultimately, the practical performance of the fabricated device is governed by its energy and power densities, which serve as key indicators of overall efficiency (Fig. 6d). The asymmetric supercapacitor device exhibits an energy density up to 0.76 mWh cm^{-2}, corresponding to a power density of 9.3 mW cm^{-2}. The results of this comparative analysis demonstrate that the fabricated asymmetric device exhibits superior efficiency compared with other reported devices such as Co_9S_8@PPy@NiCo-LDH//AC (0.8 mW cm^{-2}, 0.132 mWh cm^{-2}),[44] Ni–Co LDH//OCC (0.435 mWh cm^{-2}, 6.01 mWcm^{-2}),[45] CoNi-2//AC (0.5 mWh cm^{-2}, 1.6 mW cm^{-2}),[46] s-NiCo LDH//AC (0.46 mWh cm^{-2}, 4.5 mW cm^{-2}),[36] NC LDH NFAs@NSs/Ni//AC@CF (0.40 mWh cm^{-2}, 2.40 mW cm^{-2}),[47] and NiCo-LDH@NiSe/NF//AC/NF (0.454 mWh cm^{-2}, 4 mW cm^{-2}).[33]

The stability of the device was evaluated by subjecting it to 10 000 charge–discharge cycles (Fig. 6e). As shown in the inset of Fig. 6e, the galvanostatic charge–discharge curves of NiCoAl-2-LDH@3D-PE//ATCC at a current density of 10 mA cm^{-2} for the initial and final cycles are nearly identical, with only a slight decrease in the discharge time. This observation confirms the outstanding cycling stability of the fabricated device. The device maintains 95.21% of its initial capacitance even after 10 000 continuous charge–discharge cycles, demonstrating remarkable long-term cycling stability. Nyquist plot analysis shows a slight rise in the device's charge transfer resistance after extended cycling tests, which corroborates the slight reduction observed in the device's capacitance performance (Fig. 6f). These findings demonstrate the outstanding long-term cycling stability of the fabricated asymmetric device. To demonstrate practical applicability and scalability, two identical two asymmetric 0.8mm-thick-NiCoAl-LDH@3D-PE/ATCC supercapacitor cells were connected in series and charged to 3.0 V. The two-cell assembly was able to continuously power a standard LED for over 45 minutes after being disconnected from the charger (see SI Movie S1). This demonstration verifies that our 3D-printed electrode architecture can be assembled modularly to increase operating voltage and deliver sustained energy to a small electronic device under ambient conditions.

Conclusion

This study demonstrates the use of a 3D-printed carbon-based skeleton (3D-PE) as a robust scaffold for NiCoAl-LDH@3D-PE cathodes. At first, incorporation of aluminum (Al) enlarged the LDH interlayer spacing, exposed more active sites, and accelerated redox kinetics, leading to enhanced specific capacitance (1968 *vs.* 1762 F g^{-1}) and improved cycling stability (94% *vs.* 85% after 5000 cycles). Since Al does not participate in redox

reactions, it also helps stabilize the LDH lattice, further enhancing the electrode's long-term durability. To address sluggish ion diffusion in thick electrodes, the NiCoAl-LDH@3D-PE thickness was increased from 0.8 mm to 3.2 mm. The areal capacitance increased proportionally (12.1 to 49.9 F cm^{-2}) while gravimetric capacitance remained constant, enabled by the orthogonal 3D-PE architecture that preserves electron pathways and allows uniform LDH infiltration and deposition. The 3.2 mm electrode achieved a high mass loading of 28.28 mg cm^{-2}, mitigating ion transport limitations even at large thickness. The assembled asymmetric device (NiCoAl-2-LDH@3D-PE//ATCC) delivered 0.76 mWh cm^{-2} at 9.3 mW cm^{-2} and retained 95.2% of its capacitance after 10 000 cycles, highlighting the synergy of Al-optimized LDH and 3D-printed scaffolds for scalable, high-performance supercapacitors.

Conflicts of interest

The authors declare no competing financial interest.

Abbreviations

PLA	Polylactic acid
NiCoAl-LDH	Nickel-cobalt-Aluminum-layered double hydroxide
ASC	Asymmetric supercapacitors
3D-PEs	3D-printed electrodes.

Data availability

The data supporting this article have been included as part of the supplementary information (SI). Supplementary information: Fig. S1: (a) SEM image of cross-sectional NiCoAl-2-LDH@3D-PE. Fig. S2: The high-resolution XPS spectra of Ni 2p (a), Co 2p (b), and O 1s (c) for NiCo-LDH@3D-PE. Fig. S3: The high-resolution XPS spectra of Ni 2p (a), Co 2p (b), Al 2p (c), and O 1s (d) for NiCoAl-LDH-5@3D-PE. Fig. S4: Raman spectra of 3D-PE and NiCoAl-2-LDH@3D-PE. Fig. S5: (a) CV curves response for different scan rates at NiCoAl-2-LDH@3D-PE. (b) Calibration plot for $\log(\nu/\text{mV s}^{-1})$ *vs.* $\log(i_p/\text{A cm}^{-2})$. (c) Bar graph for contribution percentage between capacitive and diffusion-limited capacitances at different scan rates. Fig. S6: Niquist plots of NiCo-LDH@3D-PE, NiCoAl-2-LDH@3D-PE, NiCoAl-5-LDH@3D-PE. Fig. S7: Nyquist plot of 3D printed electrode before and after calcination. Fig. S8: (a) N2 adsorption isotherms and (b) BJH curves of 3D-PE, NiCo-LDH@3D-PE, NiCoAl-2-LDH@3D-PE, and NiCoAl-5-LDH@3D-PE. Fig. S9: (a) CV curves of NiCoAl-2-LDH@3D-PE with different scan rate, (b) CV curves of 3D-PE, NiCo-LDH@3D-PE, NiCoAl-2-LDH@3D-PE, and NiCoAl-5-LDH@3D-PE. GCD curves with different current density of (c) NiCo-LDH@3D-PE, (d) NiCoAl-2-LDH@3D-PE, (e) NiCoAl-5-LDH@3D-PE. Fig. S10: GCD curves at different current densities of NiCoAl-2-LDH@3D-PE with the thickness of (a) 0.8 mm, (b) 1.6 mm, (c) 2.4 mm, and (d) 3.2 mm. Fig. S11: Nyquist plots of NiCoAl-LDH-2@3D-PE with different electrode thickness. Fig. S12: Electrochemical performance of ATCC: (a and b) CV and GCD curves at different scan rate and different current densities. (c) Nyquist plot for ATCC. (d) Areal capacitance for different current densities. Fig. S13: digital images of 2 asymmetric supercapacitor devices NiCoAl-2-LDH@3D-PE//ATCC. Fig. S14: schematic illustration of ion and electron transport pathways within the 3D-PE structure. Table S1: BET surface area, pore volume and mean pore diameter of 3D-PE and NiCoAl-2-LDH@3D-PE. Table S2: R_{esr} and R_{ct} of NiCoAl-LDH-2@3D-PE with different electrode thickness. Video S1: Two asymmetric supercapacitor devices, NiCoAl-2-LDH@3D-PE//ATCC, power the LED. See DOI: https://doi.org/10.1039/d5nr03834k.

Acknowledgements

This research was supported by the National Research Foundation (NRF) grant funded by the Korean government (MSIT) (RS-2023-00223501, RS-2024-00407053, and RS-2025-00518479). This research was also supported by Korea Planning & Evaluation Institute of Industrial Technology (KEIT) grant funded by the Korea Government (MOTIE) (RS-2024-00443773).

References

1 W. Zuo, R. Li, C. Zhou, Y. Li, J. Xia and J. Liu, Battery-Supercapacitor Hybrid Devices: Recent Progress and Future Prospects, *Adv. Sci.*, 2017, **4**(7), 1600539.
2 R. F. Service, New 'Supercapacitor' Promises to Pack More Electrical Punch, *Science*, 2006, **313**(5789), 902–902.
3 P. Simon and Y. Gogotsi, Materials for electrochemical capacitors, *Nat. Mater.*, 2008, **7**(11), 845–854.
4 Y. Kuang, C. Chen, D. Kirsch and L. Hu, Thick Electrode Batteries: Principles, Opportunities, and Challenges, *Adv. Energy Mater.*, 2019, **9**(33), 1901457.
5 Z. Li, X. Wang, Z. Wang, L. Wang, Y. Guo, C. Zhou, X. Li, K. Du and Y. Luo, Nickel-cobalt layered double hydroxide nanosheets anchored to the inner wall of wood carbon tracheids by nitrogen-doped atoms for high-performance supercapacitors, *J. Colloid Interface Sci.*, 2022, **608**, 70–78.
6 V. Ruiz, C. Blanco, R. Santamaría, J. M. Ramos-Fernández, M. Martínez-Escandell, A. Sepúlveda-Escribano and F. Rodríguez-Reinoso, An activated carbon monolith as an electrode material for supercapacitors, *Carbon*, 2009, **47**(1), 195–200.
7 A. Garcia-Gomez, P. Miles, T. A. Centeno and J. M. Rojo, Uniaxially oriented carbon monoliths as supercapacitor electrodes, *Electrochim. Acta*, 2010, **55**(28), 8539–8544.
8 W. Yao, D. Zheng, Z. Li, Y. Wang, H. Tan and Y. Zhang, MXene@ carbonized wood monolithic electrode with hier-

archical porous framework for high-performance supercapacitors, *Appl. Surf. Sci.*, 2023, **638**, 158130.

9 Y. Hu, J. Ouyang, W. Xiong, R. Wang, Y. Lu, W. Yin, Y. Fan, Z. Li, K. Du, X. Li, *et al.*, A 3D stacked corrugated pore structure composed of CoNiO2 and polyaniline within the tracheids of wood-derived carbon for high-performance asymmetric supercapacitors, *J. Colloid Interface Sci.*, 2023, **648**, 674–682.

10 B. Yao, S. Chandrasekaran, J. Zhang, W. Xiao, F. Qian, C. Zhu, E. B. Duoss, C. M. Spadaccini, M. A. Worsley and Y. Li, Efficient 3D Printed Pseudocapacitive Electrodes with Ultrahigh MnO_2 Loading, *Joule*, 2019, **3**(2), 459–470.

11 W. Yang, J. Yang, J. J. Byun, F. P. Moissinac, J. Xu, S. J. Haigh, M. Domingos, M. A. Bissett, R. A. W. Dryfe and S. Barg, 3D Printing of Freestanding MXene Architectures for Current-Collector-Free Supercapacitors, *Adv. Mater.*, 2019, **31**(37), 1902725.

12 C. Zhao, C. Wang, R. Gorkin, S. Beirne, K. Shu and G. G. Wallace, Three dimensional (3D) printed electrodes for interdigitated supercapacitors, *Electrochem. Commun.*, 2014, **41**, 20–23.

13 X. Li, D. Du, Y. Zhang, W. Xing, Q. Xue and Z. Yan, Layered double hydroxides toward high-performance supercapacitors, *J. Mater. Chem. A*, 2017, **5**(30), 15460–15485, DOI: 10.1039/C7TA04001F.

14 J. Yang, C. Yu, X. Fan and J. Qiu, 3D Architecture Materials Made of NiCoAl-LDH Nanoplates Coupled with NiCo-Carbonate Hydroxide Nanowires Grown on Flexible Graphite Paper for Asymmetric Supercapacitors, *Adv. Energy Mater.*, 2014, **4**(18), 1400761.

15 T. C. Doan, B. Muthukutty and H. Yoo, High mass-loading of nickel-cobalt layered double hydroxide on 3D-printed electrode for cathode of asymmetric supercapacitor, *Journal of Energy Storage*, 2023, **68**, 107648.

16 X. Gao, X. Liu, D. Wu, B. Qian, Z. Kou, Z. Pan, Y. Pang, L. Miao and J. Wang, Significant Role of Al in Ternary Layered Double Hydroxides for Enhancing Electrochemical Performance of Flexible Asymmetric Supercapacitor, *Adv. Funct. Mater.*, 2019, **29**(36), 1903879.

17 X. Hong, H. You, C. Deng, G. Wang and W. Dong, Optimization of Al-doped NiCo2O4 hybrid nanostructures and their electrochemical activation feature in supercapacitors, *J. Alloys Compd.*, 2024, **1002**, 175239.

18 Z. Miao, Y. Huang, J. Xin, X. Su, Y. Sang, H. Liu and J.-J. Wang, High-Performance Symmetric Supercapacitor Constructed Using Carbon Cloth Boosted by Engineering Oxygen-Containing Functional Groups, *ACS Appl. Mater. Interfaces*, 2019, **11**(19), 18044–18050.

19 B. Fang, Y. Z. Wei, K. Suzuki and M. Kumagai, Surface modification of carbonaceous materials for EDLCs application, *Electrochim. Acta*, 2005, **50**(18), 3616–3621.

20 B. Geng, W. Hu, X. Wu, M. Du, G. Shan and Q. Zheng, NiCoAl Ternary Metal Hydroxides Prepared by Fluorine Ion Assisted Electrodeposition Process for Long Lifespan Supercapacitor Electrodes, *J. Electrochem. Soc.*, 2022, **169**, 082521.

21 A. K. Trivedi and M. K. Gupta, PLA based biodegradable bionanocomposite filaments reinforced with nanocellulose: development and analysis of properties, *Sci. Rep.*, 2024, **14**(1), 23819.

22 X. Han, J. Li, J. Lu, S. Luo, J. Wan, B. Li, C. Hu and X. Cheng, High mass-loading NiCo-LDH nanosheet arrays grown on carbon cloth by electrodeposition for excellent electrochemical energy storage, *Nano Energy*, 2021, **86**, 106079.

23 X. Xuan, M. Qian, L. Han, L. Wan, Y. Li, T. Lu, L. Pan, Y. Niu and S. Gong, *In situ* growth of hollow NiCo layered double hydroxide on carbon substrate for flexible supercapacitor, *Electrochim. Acta*, 2019, **321**, 134710.

24 X. Wang, Y. Lin, Y. Su, B. Zhang, C. Li, H. Wang and L. Wang, Design and synthesis of ternary-component layered double hydroxides for high-performance supercapacitors: understanding the role of trivalent metal ions, *Electrochim. Acta*, 2017, **225**, 263–271.

25 X. Lu, H. Xue, H. Gong, M. Bai, D. Tang, R. Ma and T. Sasaki, 2D Layered Double Hydroxide Nanosheets and Their Derivatives Toward Efficient Oxygen Evolution Reaction, *Nano-Micro Lett.*, 2020, **12**(1), 86.

26 A. Liu and J. R. Dahn, The Formation of Layered Double Hydroxide Phases in the Coprecipitation Syntheses of [Ni0.80Co0.15](1−x)/0.95Alx(OH)2(anionn−)x/n (x = 0–0.2, n = 1, 2), *ChemEngineering*, 2019, **3**, 38.

27 Y. Chen, Y. Ouyang, J. Yang, L. Zheng, B. Chang, C. Wu, X. Guo, G. Chen and X. Wang, Facile Preparation and Performances of Ni, Co, and Al Layered Double Hydroxides for Application in High-Performance Asymmetric Supercapacitors, *ACS Appl. Energy Mater.*, 2021, **4**(9), 9384–9392.

28 H. M. Sun, Y. X. Ye, Z. F. Tian, S. L. Wu, J. Liu and C. H. Liang, Ni3+ doped cobalt–nickel layered double hydroxides as high-performance electrode materials for supercapacitors, *RSC Adv.*, 2017, **7**(77), 49010–49014, DOI: 10.1039/C7RA09427B.

29 Z. Yuan, H. Wang, J. Shen, P. Ye, J. Ning, Y. Zhong and Y. Hu, Hierarchical Cu2S@NiCo-LDH double-shelled nanotube arrays with enhanced electrochemical performance for hybrid supercapacitors, *J. Mater. Chem. A*, 2020, **8**(42), 22163–22174, DOI: 10.1039/D0TA08006C.

30 X. Wang, H. Li, H. Li, S. Lin, J. Bai, J. Dai, C. Liang, X. Zhu, Y. Sun and S. Dou, Heterostructures of Ni–Co–Al layered double hydroxide assembled on V4C3 MXene for high-energy hybrid supercapacitors, *J. Mater. Chem. A*, 2019, **7**(5), 2291–2300, DOI: 10.1039/C8TA11249E.

31 S. P. Lonkar, J.-M. Raquez and P. Dubois, One-Pot Microwave-Assisted Synthesis of Graphene/Layered Double Hydroxide (LDH) Nanohybrids, *Nano-Micro Lett.*, 2015, **7**(4), 332–340.

32 K. K. Sarigamala, S. Shukla, A. Struck and S. Saxena, Rationally engineered 3D-dendritic cell-like morphologies of LDH nanostructures using graphene-based core–shell structures, *Microsyst. Nanoeng.*, 2019, **5**(1), 65.

33 C. Lu, Y. Yan, T. Zhai, Y. Fan and W. Zhou, 2 nm-Thick NiCo LDH@NiSe Single-Crystal Nanorods Grown on Ni

Foam as Integrated Electrode with Enhanced Areal Capacity for Supercapacitors, *Batteries Supercaps*, 2020, **3**(6), 534–540.

34 L. Dai, S. Peng, X. Wang, B. Chen, Y. Wu, Q. Xie and Y. Ruan, Three-dimensional NiCoS nanotubes@NiCo-LDH nanosheets core–shell heterostructure for high-rate capability alkaline zinc-based batteries, *RSC Adv.*, 2024, **14**(12), 7999–8006, DOI: 10.1039/D4RA00521J.

35 G. Wang, Z. Jin and W. Zhang, A phosphatized NiCo LDH 1D dendritic electrode for high energy asymmetric supercapacitors, *Dalton Trans.*, 2019, **48**(39), 14853–14863, DOI: 10.1039/C9DT02955A.

36 T. Yang, J. Ye, S. Chen, S. Liao, H. Chen, L. Yang, X. Xu and F. Wang, Construction of nanowall-supported-nanorod nico ldh array electrode with high mass-loading on carbon cloth for high-performance asymmetric supercapacitors, *Electrochim. Acta*, 2020, **362**, 137081.

37 J. Xing, J. Du, X. Zhang, Y. Shao, T. Zhang and C. Xu, A Ni-P@NiCo LDH core–shell nanorod-decorated nickel foam with enhanced areal specific capacitance for high-performance supercapacitors, *Dalton Trans.*, 2017, **46**(30), 10064–10072, DOI: 10.1039/C7DT01910F.

38 X. Gao, R. Zhang, X. Huang, Y. Shi, C. Wang, Y. Gao and Z. Han, One-step growth of NiCoAl layered double hydroxides microspheres toward high energy density supercapacitors, *J. Alloys Compd.*, 2021, **859**, 157879.

39 D. Guo, X. Song, L. Tan, H. Ma, W. Sun, H. Pang, L. Zhang and X. Wang, A facile dissolved and reassembled strategy towards sandwich-like rGO@NiCoAl-LDHs with excellent supercapacitor performance, *Chem. Eng. J.*, 2019, **356**, 955–963.

40 C. Chen, Y. Zhang, Y. Li, J. Dai, J. Song, Y. Yao, Y. Gong, I. Kierzewski, J. Xie and L. Hu, All-wood, low tortuosity, aqueous, biodegradable supercapacitors with ultra-high capacitance, *Energy Environ. Sci.*, 2017, **10**(2), 538–545, DOI: 10.1039/C6EE03716J.

41 F. Wang, X. Liu, G. Duan, H. Yang, J. Y. Cheong, J. Lee, J. Ahn, Q. Zhang, S. He, J. Han, *et al.*, Wood-Derived, Conductivity and Hierarchical Pore Integrated Thick Electrode Enabling High Areal/Volumetric Energy Density for Hybrid Capacitors, *Small*, 2021, **17**(35), 2102532.

42 L. Wang, R. Wang, J. Ouyang, Z. Liu, Y. Tian, M. Cheng, Y. Wang, W. Yin, Y. Geng, Z. Wu, *et al.*, Nitrogen-Doping-Driven 3D Interwoven Nickel–Cobalt Layered Double Hydroxides on Wood Tracheid Inner Walls for Ultrahigh Areal Capacitance Supercapacitors, *ACS Appl. Energy Mater.*, 2025, **8**(16), 12128–12138.

43 L. Wang, J. Ouyang, Y. Tian, L. Zhou, M. Cheng, Y. Wang, X. Ren, Z. Wu, W. Yin, Q. Sheng, *et al.*, N-doped wood carbon electrodes with ultra-high mass loading of nickel cobalt layered hydroxides for high-performance asymmetric supercapacitors, *Appl. Surf. Sci.*, 2025, **680**, 161390.

44 L. Wang, S. Li, F. Huang, X. Yu, M. Liu and H. Zhang, Interface modification of hierarchical Co9S8@NiCo layered dihydroxide nanotube arrays using polypyrrole as charge transfer layer in flexible all-solid asymmetric supercapacitors, *J. Power Sources*, 2019, **439**, 227103.

45 M. Pan, W. Zeng, H. Quan, J. Cui, Y. Guo, Y. Wang and D. Chen, Low-crystalline Ni/Co-oxyhydroxides nanoarrays on carbon cloth with high mass loading and hierarchical structure as cathode for supercapacitors, *Electrochim. Acta*, 2020, **357**, 136886.

46 J.-J. Zhou, W. Ji, L. Xu, Y. Yang, W. Wang, H. Ding, X. Xu, W. Wang, P. Zhang, Z. Hua, *et al.*, Controllable transformation of CoNi-MOF-74 on Ni foam into hierarchical-porous Co(OH)2/Ni(OH)2 micro-rods with ultra-high specific surface area for energy storage, *Chem. Eng. J.*, 2022, **428**, 132123.

47 G. Nagaraju, S. Chandra Sekhar, L. Krishna Bharat and J. S. Yu, Wearable Fabrics with Self-Branched Bimetallic Layered Double Hydroxide Coaxial Nanostructures for Hybrid Supercapacitors, *ACS Nano*, 2017, **11**(11), 10860–10874.

48 J. Bae, Master's thesis, Hanyang University ERICA, 2025.